ELSEVIER

Transport of particles in fluids

Hans J. Herrmann[*],[1],[2], José S. Andrade Jr., Ascânio D. Araújo, Murilo P. Almeida

Departamento de Física, Universidade Federal do Ceará, 60451-970 Fortaleza, Ceará, Brazil

Available online 11 September 2006

Abstract

The interaction of moving fluids with particles is still only understood phenomenologically when the Reynolds number is not vanishing. I will present three different numerical studies all using the solver "fluent" which elucidate this issue from different points of view. On one hand, I will consider the case of fixed particles, i.e., a porous medium and present the distribution of channel openings, fluid velocities and fluxes. These distributions show a scaling law in the density of particles and for the fluxes follow an unexpected stretched exponential behavior. The next issue will be filtering, i.e., the release of massive tracer particles within this fluid. Interestingly, a critical Stokes number exists below which no particles are captured and which is characterized by a critical exponent of $\frac{1}{2}$. Finally, I will also show data on saltation, i.e., the motion of particles on a surface which when dragged by the fluid performs jumps. This is the classical eolian transport mechanism responsible for dune formation. The empirical relations between flux and wind velocity are reproduced and a scaling law of the deformed wind profile is presented.
© 2006 Elsevier B.V. All rights reserved.

Keywords: Granular matter; Drag; Saltation; Filters; Porous media

1. Introduction

Many applications in chemical engineering, fluid mechanics, geology and biology involve systems of particles immersed in a flowing liquid or gas [1–3]. Also fluid flow through a porous medium is of importance in many practical situations ranging from oil recovery to chemical reactors and has been studied experimentally and theoretically for a long time [4–6]. Due to disorder, porous media display many interesting properties that are, however, difficult to handle even numerically. One important feature is the presence of heterogeneities in the flux intensities due to varying channel widths. They are crucial to understand stagnation, filtering, dispersion and tracer diffusion.

The fluid mechanics in the porous space is based on the assumption that a Newtonian and incompressible fluid flows under steady-state conditions. The Navier–Stokes and continuity equations for this case reduce to

$$\rho \vec{u} \cdot \nabla \vec{u} = -\nabla p + \mu \nabla^2 \vec{u}, \tag{1}$$

$$\nabla \cdot \vec{u} = 0, \tag{2}$$

where $\vec{u}$ and p are the local velocity and pressure fields, respectively, and ρ is the density of the fluid. No-slip boundary conditions are applied along the entire solid–fluid interface, whereas a uniform velocity profile, $u_x(0, y) = V$ and $u_y(0, y) = 0$, is imposed at the in-let of the channel. For simplicity, we restrict our study to the case where the Reynolds number, defined here as $Re \equiv \rho V L_y / \mu$, is sufficiently low ($Re < 1$) to ensure a laminar viscous regime for fluid flow. We use FLUENT [7], a computational fluid dynamic solver, to obtain the numerical solution of Eqs. (1) and (2) on a triangulated grid of up to hundred thousand points adapted to the geometry of the porous medium.

The traditional approach for the investigation of single-phase fluid flow at low Reynolds number in disordered porous media is to characterize the system in terms of Darcy's law [4,6], which assumes that a *macroscopic* index, the permeability K, relates the average fluid velocity V through the pores with the pressure drop ΔP measured across the system,

$$V = -\frac{K}{\mu}\frac{\Delta P}{L}, \tag{3}$$

where L is the length of the sample in the flow direction and μ the viscosity of the fluid. In previous studies [9–15], computational simulations based on detailed models of pore geometry and fluid flow have been used to predict permeability coefficients.

In this paper, we present numerical calculations for a fluid flowing through a two-dimensional channel of width L_y and length L_x filled with randomly positioned circular obstacles [16]. For instance, this type of model has been frequently used to study flow through fibrous filters [30]. Here, the fluid flows in the x-direction at low but non-zero Reynolds number, and in the y-direction we impose periodic boundary conditions. We consider a particular type of random sequential adsorption (RSA) model [18] in two dimensions to describe the geometry of the porous medium. As shown in Fig. 1, disks of diameter D are placed randomly by first choosing from a homogeneous distribution between $D/2$ and $L_x - D/2(L_y - D/2)$ the random $x-(y-)$ coordinates of their center. If the disk allocated at this position is separated by a distance smaller than $D/10$ or overlaps with an already existing disk, this attempt of placing a disk is rejected and a new attempt is made. Each successful placing constitutes a decrease in the porosity (void fraction) ε by $\pi D/4L_xL_y$. One can associate this filling procedure to a temporal evolution and identify a successful placing of a disk as one time step. By stopping this procedure when a certain value of ε is achieved, we can produce in this way systems of well-controlled porosity. We study in particular configurations with $\varepsilon = 0.6$, 0.7, 0.8 and 0.9.
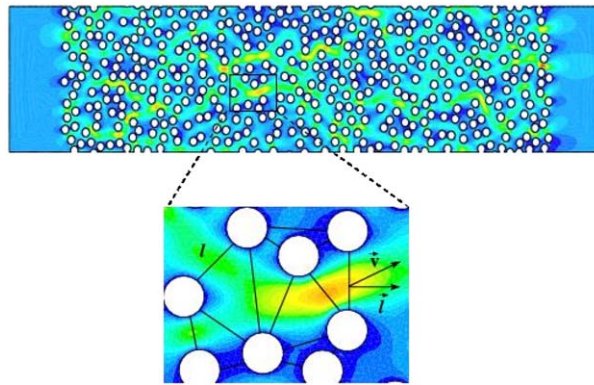

Fig. 1. Contour plot of the velocity magnitude for a typical realization of a pore space with porosity $\varepsilon = 0.7$ subjected to a low Reynolds number and periodic boundary conditions applied in the y-direction. The fluid is pushed from left to right. The colors ranging from blue (dark) to red (light) correspond to low and high velocity magnitudes, respectively. The close-up shows a typical pore opening of length l across which the fluid flows with a line average velocity v. The local flux at the pore opening is given by $q = vl\cos\theta$, where θ is the angle between v and the vector normal to the line connecting the two disks.

2. Distributions of flux in porous medium

First, we analyze the geometry of our random configurations making a Voronoi construction of the point set given by the centers of the disks [19,20]. We define two disks to be neighbors of each other if they are connected by a bond of the Voronoi tessellation. These bonds constitute therefore the openings or pore channels through which a fluid can flow when it is pushed through our porous medium, as can be seen in the close-up of Fig. 1. We measure the channel widths l as the length of these bonds minus the diameter D, and plot in Fig. 2 the (normalized) distributions of the normalized channel widths $l^* = l/D$ for the four different porosities. Clearly one notices two distinct regimes: (i) for large widths l^* the distribution decays are seemingly exponentially with l^*, and (ii) for small l^* it has a strong dependence on the porosity, increasing dramatically at the origin with decreasing porosity. The crossover between the two regimes is visible as a peak which shifts between $\varepsilon = 0.9$ and 0.8 and then stays for smaller porosities at about $l^* = 1$, i.e., $l = D$. These distribution functions can be qualitatively understood in the following way. For very large porosities, i.e., very dilute systems, the distance between the particles is essentially uncorrelated due to excluded volume and is therefore Gaussian distributed around a mean value $\langle l \rangle$.

If for simplicity one imagines particles being on a regular triangular lattice as an idealized configuration in two dimensions, the following expression is obtained:

$$\langle l \rangle = D\left(\sqrt{\frac{\pi}{2\sqrt{3}(1-\varepsilon)}} - 1 \right). \tag{4}$$

The filling process will strongly feel the clogging due to excluded volume when one disk just fits into the hole between three disks. This situation occurs when $\langle l \rangle = D(\sqrt{3} - 1)$. Inserting this into Eq. (4) gives a crossover porosity of $\varepsilon = 1 - \pi/6\sqrt{3} \approx 0.7$ which agrees with our simulation (see Fig. 2). Interestingly, a related property, namely the correlation function, does not seem to show such a crossover [21,22]. For sufficiently large values of l, all distributions $P(l)$ collapse to a single curve when rescaled by the corresponding value of $\langle l \rangle$ calculated from Eq. (4). This result indicates that our simple description based on a diluted system of particles placed on a regular lattice provides a good approximation for the geometry of the disordered porous medium.

Simulations have been performed [29] by averaging over 10 different pore space realizations generated for each value of porosity. The contour plot in Fig. 1 of the local velocity magnitude for a typical realization of the porous medium with porosity $\varepsilon = 0.7$ clearly reveals that the transport of momentum through the complex
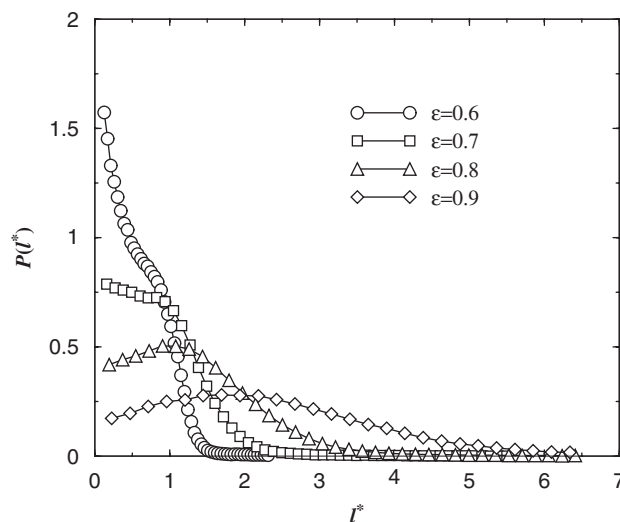

Fig. 2. Distributions of the normalized channel widths $l^* = l/D$ for different values of porosity ε. From left to right, the two vertical dashed lines indicate the values of the minimum distance between disks $l^* = 0.1$ and the size of the disks $l^* = l$.

geometry generates preferential channels [15]. Once the numerical solution for the velocity and pressure fields in each cell of the numerical grid is obtained, we compute the fluid velocity magnitudes v associated to each channel. This value is the magnitude of the *line average velocity vector* $\vec{v}$ calculated as the average over the local velocity vectors $\vec{u}$ along the corresponding channel width l.

In Fig. 3, we show the data collapse of all distributions of normalized velocity magnitudes $P(v^*)$, where $v^* = v/V$, obtained by rescaling the variable v^* with the corresponding value of ε^{-2}. It is also interesting to note that these rescaled distributions follow a typical Gaussian behavior except for very small $v^*\varepsilon^2$, as indicated by the solid line in Fig. 3. The average interstitial velocity also scales with the porosity as $(v)\sim\varepsilon^{-2}$, confirming the rescaling procedure adopted to obtain the collapse of the distributions $P(v^*)$ in the main plot of Fig. 3. Plotting for each channel v against l gives a cloud of points which for all considered values of ε results in a rather unexpected least-square fit relation of the type $v\sim\sqrt{l}$.

We now analyze the distribution of fluxes throughout the porous medium. Each local flux q crossing its corresponding pore opening l is given by $q = vl \cos \theta$, where θ is the angle between v and the vector normal to the cross-section of the channel (see Fig. 1). In Fig. 4, we show that the distributions of normalized fluxes $\varphi = q/q_t$, where $q_t = VL_y$ is the total flux, have a stretched exponential form:

$$P(\phi)\sim \exp(-\sqrt{\phi/\phi_0}), \qquad\qquad (5)$$

with $\phi_0 \approx 0.005$ being a characteristic value. This simple form of Eq. (5) is quite unexpected considering the rather complex dependence of $P(l)$ on ε. Moreover, all flux distributions $P(\phi)$ collapse on top of each other when rescaled by the corresponding value of $\langle l^* \rangle^{-1}\varepsilon^2$. This collapse for distinct porous media results from the fact that mass conservation is imposed at the microscopic level of the geometrical model adopted here, which is microscopically disordered, but at a larger scale is macroscopically homogeneous [6].

3. Filtration

Filtration is not only the basic mechanism to get clean air or water but also plays a crucial role in the chemical industry. For this reason, it has been studied extensively in the past [23]. In particular, we will focus here on deep bed filtration where the particles in suspension are much smaller than the pores of the filter which they penetrate until being captured at various depths. For non-Brownian particles, at least four capture mechanisms can be distinguished, namely, the geometrical, the chemical, the gravitational and the hydrodynamical process [23].
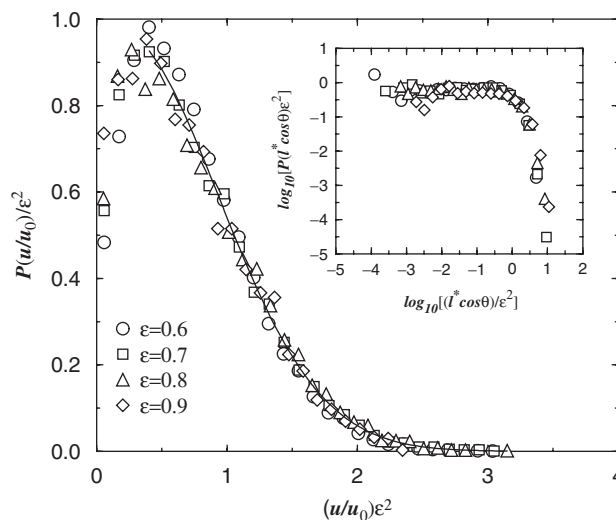

Fig. 3. Double-logarithmic plot of the distributions of the local normalized velocity magnitudes v^*, i.e., v/V, multiplied by ε^2 as explained in the text. The solid line is a Gaussian fit. The inset shows the distribution of the channel width multiplied by the cosine of the angle θ as defined in Fig. 1.
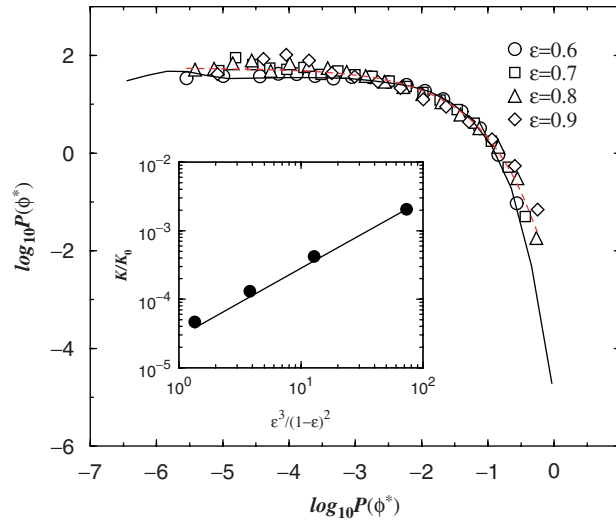
Fig. 4. Log–log plot of the distributions of the normalized local fluxes $\varphi = q/q_t$ for different porosities e. The (red) dashed line is a fit of the form $\exp(-\sqrt{\phi/\phi_0})$, where $\varphi_0 \approx 0.005$. In the inset, we see a double-logarithmic plot of the global flux and the straight line verifies the Kozeny–Carman equation.

In the past, very carefully controlled laboratory experiments were conducted by Ghidaglia et al. [24] evidencing a sharp transition in particle capture as function of the dimensionless ratio of particle to pore diameter characterized by the divergence of the penetration depth. Using a capillary network to model the pore space morphology, they showed that this transition does not belong to the universality class of percolation, contrary to what simple geometrical considerations would suggest. Subsequently, Lee and Koplik [25] found a transition from an open to a clogged state of the porous medium that is function of the mean particle size. Much less effort, however, has been dedicated to quantify the effect of inertial impact on the efficiency of a deep bed filter. For example, Ghidaglia et al. [24] only included this effect heuristically in their model through an ad hoc particle capture parameter.

We will concentrate here on the inertial effects in capture which constitute an important mechanism in most practical cases and, despite much effort, are quantitatively not yet understood, as reviewed in Ref. [26]. The effect of inertia on the suspended particles is usually quantified by the dimensionless *Stokes number*, $Vd_p^2\rho_p/18\ell\mu$ where d_p and ρ_p are the diameter and density of the particle, respectively, ℓ is a characteristic length of the pores, μ the viscosity and V the velocity of the fluid. Inertial capture by fixed bodies has already been described since 1940 by Taylor and proven to happen for inviscid fluids above a critical Stokes number [27]. This phenomenon has been studied on fixed, periodic arrays of rectangles and cylinders [28] without a more detailed discussion about the nature of an eventual transition. It is our aim to present a detailed hydrodynamic calculation of the inertial capture of particles in a porous medium. We disclose novel scaling relations for ordered as well as random porous structures.

We first consider the case of an infinite ordered porous medium composed of a periodic arrangement of fixed circular obstacles (e.g., cylinders) [29]. This system can then be completely represented in terms of a single square cell of unitary size and porosity given by $\varepsilon = (1-\pi D^2/4)$, where D is the diameter of the obstacle, as shown in Fig. 1. Assuming Stokesian flow through the void space an analytical solution has been provided by Marshall et al. [30]. Here we use this solution to obtain the velocity flow field u and study the transport of particles numerically. For simplicity, we assume that the influx of suspended particles is so small that (i) the fluid phase is not affected by changes in the particle volume fraction and (ii) particle–particle interactions are negligible. Moreover, we also consider that the movement of the particles does not impart momentum to the flow field. Finally, if we assume that the drag force and gravity are the only relevant forces acting on the particles, their trajectories can be calculated by integration of the following equation of motion:

$$\frac{\mathrm{d}\mathbf{u}_p^*}{\mathrm{d}t*} = \frac{(\mathbf{u}^* - \mathbf{u}_p^*)}{St} + F_g \frac{\mathbf{g}}{|\mathbf{g}|}, \tag{6}$$

where $F_g \equiv (\rho_p - \rho)\ell|\mathbf{g}|/(V^2\rho_p)$ is a dimensionless parameter, $\mathbf{g}$ the gravity, t^* a dimensionless time, and $\mathbf{u}_p^*$ and $\mathbf{u}^*$ the dimensionless velocities of the particle and the fluid, respectively.

In Fig. 5, we show some trajectories calculated for particles released in the flow for $St = 0.25$. Once a particle touches the boundary of the obstacle, it gets trapped. Our objective here is to search for the position y_0 of release at the inlet of the unit cell ($x_0 = 0$) and above the horizontal axis (the dashed line in Fig. 5), below which the particle is always captured and above which the particle can always escape from the system. As depicted in Fig. 5, the particle capture efficiency can be straightforwardly defined as $\delta \equiv 2y_0$. In the limiting case where $St \to \infty$, since the particles move ballistically towards the obstacle, the particle efficiency reaches its maximum, $\delta = D$. For $St \to 0$, on the other hand, the efficiency is smallest, $\delta = 0$. In this last situation, the particles can be considered as tracers that follow exactly the streamlines of the flow, avoiding trapping at the solid matrix of the porous medium.

In Fig. 6, we show the log–log plot of the variation of δ/D with the rescaled Stokes number in the presence of gravity for three different porosities. In all cases, the variable δ increases linearly with St to subsequently reach a crossover at St_x, and finally approach its upper limit ($\delta = D$). The results of our simulations also show that $St_x \sim (\varepsilon - \varepsilon_{min})$, where ε_{min} corresponds to the minimum porosity below which the distance between inlet
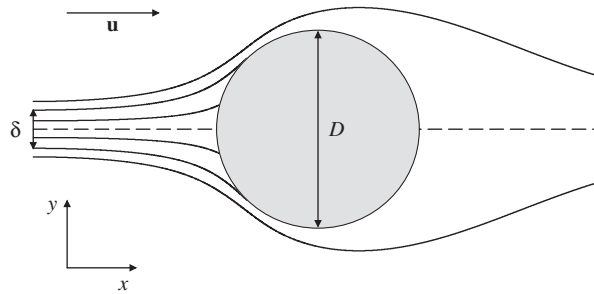

Fig. 5. Trajectories of particles released from different positions at the inlet of the periodic porous medium cell. The particles are dragged according to Eq. (6) with $St = 0.25$ and the flow field $\mathbf{u}$ is calculated from the analytical solution of Marshall et al. [30]. The thick solid lines correspond to the trajectories that limit the trapping zone in the flow.
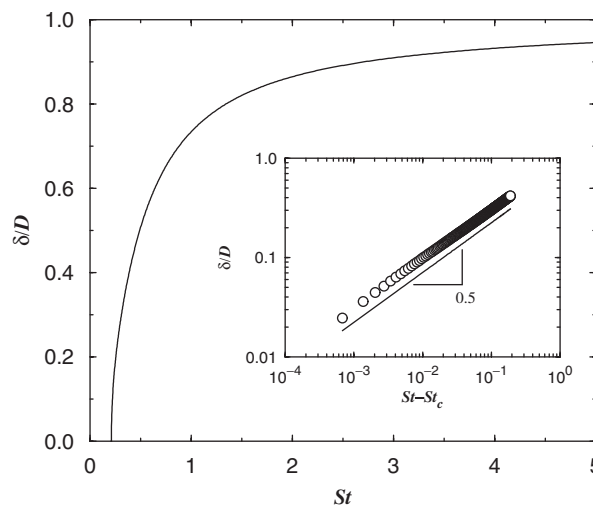

Fig. 6. Dependence of the capture efficiency δ on the rescaled Stokes number $St/(\varepsilon - \varepsilon_{min})$ for periodic porous media in the presence of gravity. Here we use $F_g = 16$, a value that is compatible with the experimental setup described in Ref. [24]. The inset shows that the behavior of the system without gravity can be characterized as a second order transition, $\delta \sim (St - St_c)^\alpha$, with $\alpha \sim 0.5$ and $St_c = 0.2679 \pm 0.0001$, 0.2096 ± 0.0001 and 0.1641 ± 0.0001, for $\varepsilon = 0.85$, 0.9 and 0.95, respectively.

and obstacle is too small for a massive particle to deviate from the obstacle. The collapse of all data shown in Fig. 6 confirms the validity of this simple rescaling approach.

The inset of Fig. 6 shows that the behavior of the system in terms of particle capture becomes significantly different in the absence of gravity. The efficiency δ remains equal to zero up to a certain critical Stokes number, St_c, that corresponds to the maximum value of St below which particles cannot be captured, regardless of the position y_0 at which they have been released. Although controversial [28], some evidence for such a finite critical point has been presented in previous analytical and numerical studies, where potential as well as viscous flow conditions have been considered [31]. Right above St_c, the variation of δ can be described in terms of a power-law, $\delta \sim (St - St_c)^\alpha$, with an exponent $\alpha \approx 0.5$. Our results show that, while the exponent α is practically independent of the porosity for $\varepsilon > 0.8$, the critical Stokes number decreases with ε, and therefore with the distance from the obstacle where the particle is released (see Fig. 6). To our knowledge, this behavior, that is typical of a second-order transition, has never been reported before for inertial capture of particles. The same result is obtained when, instead of flow in a square unit cell, we use the circular setup proposed by Kuwabara [32].

A more realistic model for the porous structure must include disorder [29]. Here we adopt a random pore space geometry that is often used to describe porous media [18]. As shown in Fig. 1, it consists of non-overlapping circular obstacles of diameter D, separated by a distance larger than $D/10$, that are randomly allocated in a two-dimensional channel of width h, until a prescribed void fraction ε is reached. For compatibility between periodic and disordered descriptions, we take the characteristic pore size to be $\ell = D/20$ (i.e., half of the minimum distance between any two obstacles of the disordered system). To reduce finite-size effects, periodic boundary conditions are applied in the y direction. Finally, end effects of the flow field are reduced by attaching a header (inlet) and a recovery (outlet) region to the two opposite faces of the channel.

The transport of momentum through the complex geometry generates typical preferential channels [15]. Once the velocity and pressure fields are obtained for the flow in the pore space, we proceed with the calculation of particle transport. When the relative velocity is low $|\mathbf{u} - \mathbf{u}_p| \ll 1$, the relation between the particle and the fluid densities is high, $\rho_p/\rho \gg 1$, and $d_p > 1\,\mu\text{m}$, except for the drag force and gravity, most of the forces acting on the particles become negligible [33]. As before, the trajectories of the particles are calculated by numerical integration of the equations of motion, but now considering a drag coefficient which is based on the empirical relation proposed by Morsi and Alexander [34].

For a fixed value of St, we consider up to 1000 particles to determine (i) whether or not these particles get trapped and (ii) the precise position at the surface of the porous matrix where their capture takes place. From these positions, as shown in the inset of Fig. 7, we plot the profiles of the fraction of non-captured particles ϕ against the longitudinal distance x along the channel. In the limiting case of a very dilute system ($\varepsilon \approx 1$) with particles being transported in the ballistic regime ($St \to \infty$), it is easy to show that $\phi(x) = \exp(-x/\lambda)$, with a penetration length given by $\lambda = \pi D/4(1 - e)$. For low and moderate values of St, the behavior of $\phi(x)$ is still exponential, but λ now being a function of the Stokes number. We postulate that the previous result can be generalized to any combination of ε and St as

$$\lambda = \pi D^2/4(1 - \varepsilon)\delta, \tag{7}$$

where the length δ is the capture efficiency analogously defined as for the periodic porous medium. As shown in Fig. 7, the penetration length follows a power-law $\lambda \sim (St)^{-\alpha}$, with a scaling exponent $\alpha \approx 1$ that is, within the numerical error bars, the same for the three values of porosity investigated. This value is also consistent with the exponent found for the periodic case with gravity.

In Fig. 7, the data collapse obtained for different values of ε reveals that the random porous system can be described very closely by the relation

$$\frac{\lambda}{D} = \frac{\beta}{St(1 - \varepsilon)}, \tag{8}$$

with a prefactor $\beta \approx 0.058$. For all practical purposes, this value is a constant for the physical model of porous geometry, flow and phenomenology of particle capture studied here.
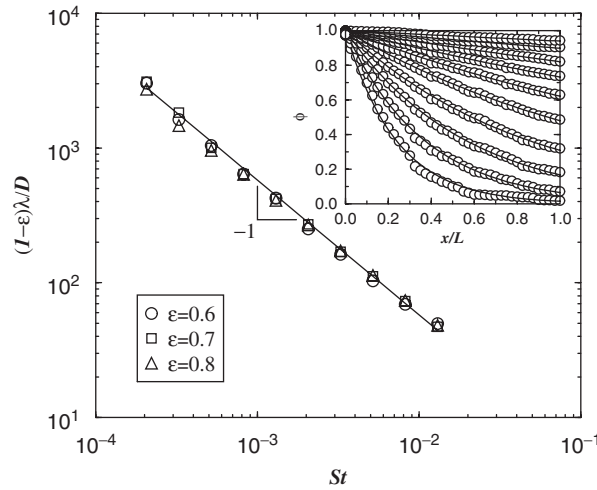
Fig. 7. Log–log plot showing the dependence of the rescaled penetration length $(1-\varepsilon)\lambda/D$ on the Stokes number St for three different porosity values. The solid line corresponds to the best fit to the data of the scaling function $(1-\varepsilon)\lambda/D = \beta St^{-\alpha}$ with the prefactor $\beta \sim 0.058$ and the exponent $\alpha = 1.00 \pm 0.02$. The inset shows the profiles of ϕ against x corresponding to a porosity $\varepsilon = 0.7$ and different values of the Stokes number. From top to bottom, $St = 2.06 \times 10^{-4}$, 3.26×10^{-4}, 5.18×10^{-4}, 8.2×10^{-4}, 1.3×10^{-3}, 2.06×10^{-3}, 3.26×10^{-3}, 5.18×10^{-3}, 8.2×10^{-3}, and 1.3×10^{-2}. The solid lines are the best fits to the different data sets of the function $\phi = exp(-x/\lambda)$, where $\lambda = \lambda(\varepsilon, St)$ is the penetration length.

4. Saltation

The transport of sand by wind is a major factor in sand encroachment, dune motion and the formation of coastal and desert landscapes. The dominating transport mechanism is saltation as first described by Bagnold [35] which consists of grains being ejected upwards, accelerated by the wind and finally impacting onto the ground producing a splash of new ejected particles. Reviews are given in Refs. [36,37]. Quantitatively, this process is however far from being understood.

Due to Newton's second law, the wind loses more momentum with increasing number of airborne particles until a saturation is reached. The maximum number of grains a wind of given strength can carry through a unit area per unit time defines the saturated flux of sand q_s. This quantity has been measured by many authors in wind tunnel experiments and on the field, and numerous empirical expressions for its dependence on the strength of the wind have been proposed [38–43]. In previous studies, theoretical forms have also been derived using approximations for the drag in turbulent flow [44,45]. All these relations are expressed as polynomials in the wind shear velocity u_* which are of third order, under the assumption that the grain hopping length scales with u_* [38,39,44–46] and otherwise can be more complex [40]. The velocity profile in a particle-laden layer has also been the object of measurement [47,48] and modellization [49]. Surprisingly, however, very few measurements of the height of the saltation layers as function of u_* have been reported [50] and no systematic data close to the threshold are available. The complete analytical treatment of this problem remains out of reach not only because of the turbulent character of the wind, but also due to the underlying moving boundary conditions in the equations of motion. More recently, a deterministic model for eolian sand transport without height dependency in the feedback has been proposed [51]. Despite much research in the past [52] there remain many uncertainties about the trajectories of the particles and their feedback with the velocity field of the wind. It is this challenge which motivated the present work and led us to discover a scaling relation for the distortion of the velocity profile.

We will present the first numerical study of saltation which solves the turbulent wind field and its feedback with the dragged particles [53]. As compared to real data, our values have no experimental fluctuations neither in the wind field nor in the particle size. As a consequence, we can determine all quantities with higher precision than ever before, and therefore with a better resolution close to the critical velocity at which the saltation process starts.

In order to get quantitative understanding of the layer of airborne particle transport above a granular surface, we simulate the situation inside a two-dimensional channel with a mobile top wall as schematically shown in Fig. 8. We impose a pressure gradient between the left and the right side. Gravity points down, i.e., in negative y-direction. The y-dependence of the pressure drop is adjusted in such a way as to insure a logarithmic velocity profile along the entire channel in the case without particles, as it is expected in fully developed turbulence [54]. More precisely, this profile follows the classical form

$$u_x(y) = (u_*/\kappa) \ln(y/y_0), \tag{9}$$

where u_x is the component of the wind velocity in the x-direction, u_* the shear velocity, $\kappa = 0.4$ is the von Karman constant and y_0 the roughness length which is typically between 10^{-4} and 10^{-2} m. The upper wall of the channel is moved with a velocity equal to the velocity of the wind at that height in order to insure a non-slip boundary condition.

The fluid mechanics inside the channel is based on the assumptions that we have an incompressible and Newtonian fluid flowing under steady state and homogeneous turbulent conditions. The fluid is air with viscosity $\mu = 1.7894 \times 10^{-5}$ kg m^{-1} s^{-1} and density $\rho = 1.225$ kg m^{-3}. The Reynolds-averaged Navier–Stokes equations with the standard k–ε model are used to describe turbulence. The numerical solution for the velocity and pressure fields is obtained through discretization by means of the control volume finite-difference technique [7]. The integral version of the governing equations is considered at each cell of the numerical grid to generate a set of non-linear algebraic equations which are linearized and solved.

After having produced a steady-state turbulent flow, we proceed with the simulation of the particle transport along the channel. Assuming that drag and gravity are the only relevant forces acting on the particles, their trajectory can be obtained by integrating the following equation of motion:

$$\frac{d\mathbf{u}_p}{dt} = F_D(\mathbf{u} - \mathbf{u}_p) + \mathbf{g}(\rho_p - \rho)/\rho_p, \tag{10}$$

where u_p is the particle velocity, $\mathbf{g}$ the gravity and $\rho_p = 2650$ kg m^{-3} a typical value for the density of sand particles. The term $F_D(\mathbf{u} - \mathbf{u}_p)$ represents the drag force per unit particle mass where

$$F_D = \frac{18\mu}{\rho_p d_p^2} \frac{C_D Re}{24}, \tag{11}$$

$d_p = 2.5 \times 10^{-4}$ m is a typical particle diameter, $Re = \rho d_p |\mathbf{u}_p - \mathbf{u}|/\mu$ is the particle Reynolds number, and the drag coefficient C_D is taken from empirical relations [34]. Each particle in our calculation represents in fact a stream of real grains. It is necessary to take into account the feedback on the local fluid velocity due to the momentum transfer to and from the particles. The momentum transfer from one phase to another is computed by adding the momentum change of every particle as it passes through a control volume [7],

$$\mathbf{F} = \sum_{\text{particles}} F_D(\mathbf{u} - \mathbf{u}_p)\dot{m}_p \Delta t, \tag{12}$$

where $\dot{m}_p$ is the mass flow rate of the particles and Δt the time step. The exchange term Eq. (12) appears as a sink in the continuous phase momentum balance.
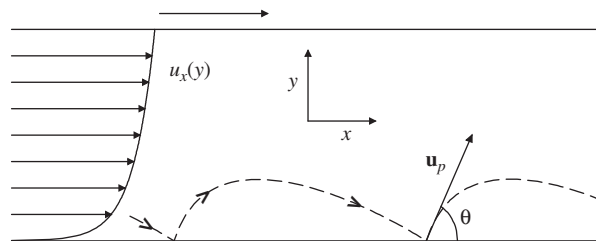

Fig. 8. Schematic representation of the setup showing the mobile wall at the top, the velocity field at different positions in the y-direction and the trajectory of a particle stream (dashed line).

In Fig. 8, we see the trajectory of one particle stream and the velocity vectors along the y-direction. Each time a particle hits the ground, it loses a fraction r of its energy and a new stream of particles is ejected at that position with an angle θ. The parameters $r = 0.84$ and $\theta = 36°$ are chosen from experimental measurements [55,56].

If u_* is below a threshold value u_t the energy loss at each impact prevails over the energy gain during the acceleration through drag and particle transport comes to a halt. Only for $u_* > u_t$ steady sand motion is achieved. The resulting flux is given by

$$q = \dot{m}_p n_p, \tag{13}$$

where n_p is the number of particle streams released. The first added particle streams are strongly accelerated in the channel and their jumping amplitude increases after each ejection until a maximum is reached. The more the particles are injected the smaller the final amplitude. Beyond a certain number n_p of particle streams, the trajectories however start to lose energy and the overall flux is reduced. This critical value n_p characterizes the saturated flux q_s through Eq. (13).

In Fig. 9, we see the plot of q_s as a function of the wind velocity u_*. Clearly, there exists a critical wind velocity threshold u_t below which no sand transport occurs at all. This agrees well with experimental observations [35,39]. Also shown in Fig. 9 is the best fit to the numerical data using the classical expression proposed by Lettau and Lettau [39],

$$q_s = C_L \frac{\rho}{g} u_*^2 (u_* - u_t), \tag{14}$$

where C_L is an adjustable parameter. We find rather good agreement using fit parameters of the same order as those of the original work [39] and a threshold value of $u_t = 0.35 \pm 0.02$. This is in fact, to our knowledge, the first time a numerical calculation is able to quantitatively reproduce this empirical expression and it confirms the validity of our simulation procedure. Other empirical relations from the literature [44–46] can also be used to fit these results. In Fig. 9, we also show that for large

$$q_s = a(u_* - u_t)^2 \tag{15}$$

fits the data better than Eq. (15), as can be seen in Fig. 9 and in particular in the inset. In the limit $u \gg u_t$, one obtains the classical behavior of Bagnold [38], as verified by the dash–dotted line in Fig. 9 and which is
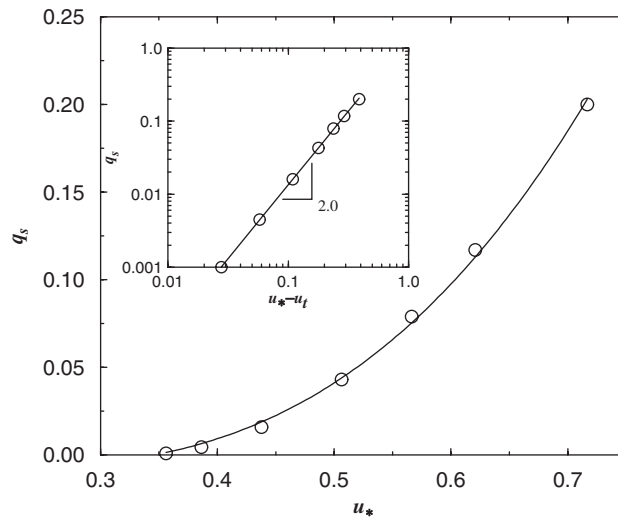

Fig. 9. Logarithmic plot of the saturated flux q_s as function of u_*. The dashed line is the fit using the expression proposed by Lettau and Lettau [39], $q_s \propto u_*^2(u_* - u_t)$, with $u_t = 0.35 \pm 0.02$. The full line corresponds to Eq. (15) and the dashed–dotted line to Bagnold's relation, $q_s \propto u$, [38]. The results shown in the inset confirm the validity of the the power-law relation Eq. (15), $q_s \propto (u_t - u_t)^2$, with the critical point given by $u_t = 0.33 \pm 0.01$.

consistent with Refs. [39,44–46]. The limit $u \ll u_t$, however, yields the quadratic relation for the flux given in Eq. (15). Physically, this is due to the fact that close to u_t the laminar component cannot be neglected.

The velocity profile of the wind within the layer of grain transport is experimentally much more difficult to access than the flux. This profile clearly deviates from the undisturbed logarithmic form of Eq. (9) because the momentum the fluid must locally exchange with the particles. In Fig. 10, we show the loss of velocity with respect to the logarithmic profile without particles of Eq. (9) for different values of q as a function of the height y. As clearly seen in Fig. 10, the loss of velocity is maximal at the same height y_{max}, regardless of the value of flux q. Except for large values of the flux, dividing the velocity axis by q, one can collapse all the profiles quite well on top of each other as can be verified in the inset of Fig. 10.

The position y_{max} of the height of maximum loss depends essentially linearly on u_* as shown in Fig. 11. This is consistent with the observation that the saltation jump length is proportional to u_* [45]. Quantitatively the
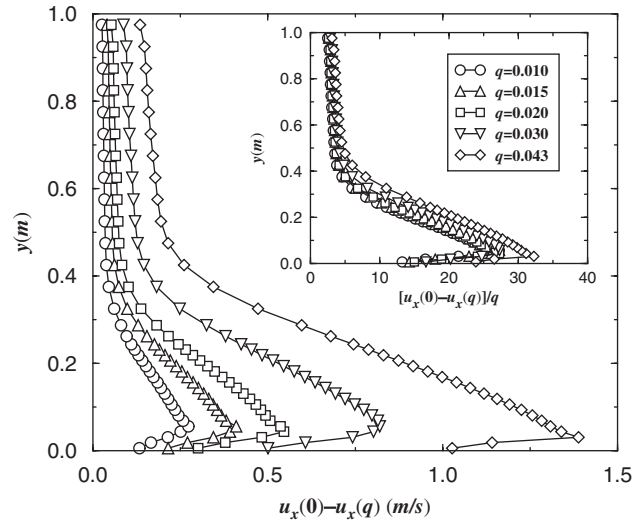

Fig. 10. Profile of the velocity difference $u_x(0) - u_x(q)$ for different values of the flux q at $u_* = 0.51$. The inset shows the data collapse of these data obtained by rescaling the velocity difference with the corresponding q.
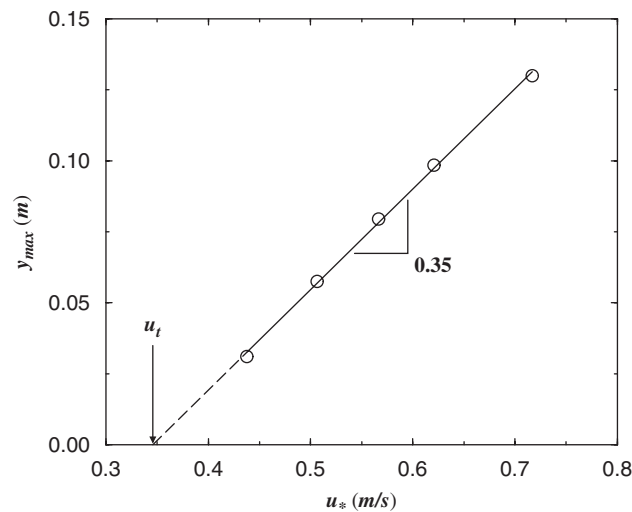

Fig. 11. Height y_{max} of the maximum loss of velocity as function of u_*. The solid line corresponds to the best linear fit to the data with a slope equal to 0.35. By extrapolation, the intercept with the x-axis provides an alternative estimate for the critical point, $u_t = 0.35$ m/s, that is consistent with the other calculations.

data in Fig. 11 also fit very well into the experiment data plots of Ref. [50] and is consistent with the analytical arguments of Ref. [45]. By extrapolation to $y_{max} = 0$, we obtain an alternative estimate for the threshold velocity, $u_t = 0.35$ m/s, that is consistent with the values calculated before from the fits to the data using Eqs. (14) and (15).

Whoever has been in the desert or on a beach during a very windy day knows that the saltation process in nature looks like a sheet of particles floating above ground at a certain height y_s which strongly depends on the wind velocity. This height corresponds to the position of the largest likelihood to find a particle as obtained from the maximum of the density profile of particles as function of height y. Fig. 11 implies that the profile of velocity difference of the wind has a minimum at a similar height, which is consistent with the maximal loss of momentum. Within the error bars, our results in fact yield that y_s coincides with the values of y_{max} in Fig. 11.

5. Conclusion

Summarizing we have found [16] that although the distribution of channel widths in a porous medium made by a two-dimensional RSA process is rather complex and exhibits a crossover at $l \sim D$, the distribution of fluxes through these channels shows an astonishingly simple behavior, namely a square-root stretched exponential distribution that scales in a simple way with the porosity. The velocity magnitudes follow a Gaussian distribution truncated at small velocities which scales with the square of the porosity. We show that our results can be macroscopically described in terms of the Kozeny–Carman relation. Future tasks consist in generalizing these studies to higher Reynolds numbers, three-dimensional models of porous media and other types of disorder.

We have also studied the phenomenon of inertial capture of particles in two-dimensional periodic as well as random porous media [29]. For the periodic model in the absence of gravity, there exists a finite Stokes number below which particles never get trapped. Furthermore, our results indicate that the transition from non-trapping to trapping with the Stokes number is of second order with a scaling exponent $\alpha \ll 0.5$. In the presence of gravity, we show that (i) this non-trapping regime is suppressed (i.e., $St_c = 0$) and (ii) the scaling exponent changes to $\alpha \ll 1$. We intend to investigate in the future the effect on the capture efficiency of simultaneous multiple particle release and the possibility of non-trapping at first contact.

Finally, we have shown results of simulations [53] giving insight about the layer of granular transport in a turbulent flow. The lack of experimental noise allows for a precise study close to the critical threshold velocity u_t that lead us to a parabolic dependence of the saturated flux. In addition, we show that the velocity profile disturbed by the presence of grains scales linearly with the flux of grains, except close to saturation. Notably a characteristic height appears at which the momentum loss in the fluid and the grain density are maximized. Moreover, this height increases linearly with the wind velocity u_*. The present model can be extended in many ways including the study of the dependence of the eolian transport layer on the grain diameter, the gas viscosity, and the solid or fluid densities. This would allow to calculate, for instance, the granular transport on Mars and compare with the expression presented in Ref. [46].

Acknowledgements

References

[1] S.L. Soo, Particles and Continuum: Multiphase Fluid Dynamics, Hemisphere, New York, 1989.
[2] D. Gidaspow, Multiphase Flow and Fluidization, Academic Press, San Diego, 1994.
[3] K. Pye, H. Tsoar, Aeolian Sand and Sand Dunes, Un-win Hyman, London, 1990.
[4] F.A.L. Dullien, Porous Media—Fluid Transport and Pore Structure, Academic, New York, 1979.
[5] P.M. Adler, Porous Media: Geometry and Transport, Butterworth-Heinemann, Stoneham, MA, 1992.
[6] M. Sahimi, Flow and Transport in Porous Media and Fractured Rock, VCH, Boston, 1995.
[7] FLUENT (trademark of FLUENT Inc.) is a commercial package for computational fluid dynamics.
[9] A. Canceliere, C. Chang, E. Foti, D.H. Rothman, S. Succi, Phys. Fluids A 2 (1990) 2085.
[10] S. Kostek, L.M. Schwartz, D.L. Johnson, Phys. Rev. B 45 (1992) 186.

[11] N.S. Martys, S. Torquato, D.P. Bentz, Phys. Rev. E 50 (1994) 403.
[12] J.S. Andrade Jr., D.A. Street, T. Shinohara, Y. Shibusa, Y. Arai, Phys. Rev. E. 51 (1995) 5725.
[13] A. Koponen, M. Kataja, J. Timonen, Phys. Rev. E 56 (1997) 3319.
[14] S. Rojas, J. Koplik, Phys. Rev. E 58 (1998) 4776.
[15] J.S. Andrade Jr., U.M.S. Costa, M.P. Almeida, H.A. Makse, H.E. Stanley, Phys. Rev. Lett. 82 (1999) 5249.
[16] A.D. Araújo, W.B. Bastos, J.S. Andrade Jr., H.J. Herrmann, Phys. Rev. E, in print.
[18] S. Torquato, Random Heterogeneous Materials: Microstructure and Macroscopic Properties, Springer, New York, 2002.
[19] G.V. Voronoi, J. Reine Angew. Math. 134 (1908) 198.
[20] D.F. Watson, Comput. J. 24 (1981) 167.
[21] S. Torquato, Phys. Rev. E 51 (1995) 3170.
[22] M.D. Rintoul, S. Torquato, G. Tarjus, Phys. Rev. E 53 (1996) 450.
[23] C. Tien, Granular Filtration of Aerosols and Hydrosols, Butterworths, Boston, 1989.
[24] C. Ghidaglia, L. de Arcangelis, J. Hinch, E. Guazzelli, Phys. Rev. E 53 (1996) R3028;
     C. Ghidaglia, L. de Arcangelis, J. Hinch, E. Guazzelli, Phys. Fluids 8 (1996) 6.
[25] J. Lee, J. Koplik, Phys. Fluids 13 (2001) 1076.
[26] D.L. Koch, R.J. Hill, Annu. Rev. Fluid Mech. 33 (2001) 619.
[27] D.E. Rosner, P. Tandon, Chem. Eng. Sci. 50 (1995) 3409.
[28] A.G. Konstandopoulos, M.J. Labowsky, D.E. Rosner, J. Aerosol Sci. 24 (1993) 471;
     M. Kostoglou, A.G. Konstandopoulos, J. Aerosol Sci. 31 (2000) 427.
[29] A.D. Araújo, J.S. Andrade Jr., H.J. Herrmann, Phys. Rev. Lett., in print.
[30] H. Marshall, M. Sahraoui, M. Kaviany, Phys. Fluids 6 (1993) 507.
[31] L.M. Levin, Izdatel'stvo Academii Nauk SSSR (1961), Eng. Transl. Foreign Techn. Div. Doc. No. FTD-HT-23-1593-67;
     N.A. Fuchs, The Mechanics of Aerosols, Pergamon, New York, 1964;
     D.B. Ingham, L.T. Hildyard, M.L. Hildyard, J. Aerosol Sci. 21 (1990) 935.
[32] S. Kubawara, J. Phys. Soc. Jpn. 14 (1959) 727.
[33] J.K. Comer, C. Kleinstreuer, C.S. Kim, J. Fluid Mech. 435 (2001) 55.
[34] S.A. Morsi, A.J. Alexander, J. Fluid Mech. 55 (1972) 193.
[35] R.A. Bagnold, The Physics of Blown Sand and Desert Dunes, Methuen, London, 1941.
[36] R.S. Anderson, M. Sørensen, B.B. Willetts, Acta Mech. 1 (Suppl.) (1991) 1.
[37] H.J. Herrmann, in: H. Hinrichsen, D. Wolf (Eds.), The Physics of Granular Media, Wiley VCH, Weinheim, 2004, pp. 233–252.
[38] R.A. Bagnold, Proc. R. Soc. London A 167 (1938) 282.
[39] K. Lettau, H. Lettau, in: H. Lettau, K. Lettau (Eds.), Exploring the World's Driest Climate, Center for Climatic Research, University of Wisconsin, Madison, 1978.
[40] B.T. Werner, J. Geol. 98 (1990) 1.
[41] K.R. Rasmussen, H.E. Mikkelsen, Acta Mech. (Suppl. 1) (1991) 135.
[42] Y.-H. Zhou, X. Guo, X.J. Zheng, Phys. Rev. E 66 (2002) 021305.
[43] J.D. Iversen, K.R. Rasmussen, Sedimentology 46 (1999) 723.
[44] P.R. Owen, J. Fluid Mech. 20 (1964) 225.
[45] M. Sørensen, in: Proceedings of the International Workshop. Physics of Blown Sand, vol. 1, University of Aarhus, Denmark, 1985, p. 141;
     M. Sørensen, Acta Mech. 1 (Suppl.) (1991) 67.
[46] B.R. White, Geophys. Res. 84 (1979) 4643.
[47] G.R. Butterfield, in: N.J. Cliffod, J.R. French, J. Hardisty (Eds.), Turbulence: Perspectives on Flow and Sediment Transport, Wiley, New York, 1993, p. 305 (Chapter 13).
[48] K. Nishimura, J.C.R. Hunt, J. Fluid. Mech. 417 (2000) 77.
[49] J.E. Ungar, P.K. Haff, Sedimentology 34 (1987) 289.
[50] Z. Dong, X. Liu, H. Wang, A. Zhao, X. Wang, Geo-morphology 49 (2002) 219.
[51] B. Andreotti, J. Fluid Mech. 510 (2004) 47.
[52] P. Nalpanis, J.C.R. Hunt, C.F. Barrett, J. Fluid Mech. 251 (1993) 661–685.
[53] M.P. Almeida, J.S. Andrade Jr., H.J. Herrmann, Phys. Rev. Lett. 96 (2006) 018001.
[54] L. Prandtl, in: W.F. Durand (Ed.), Aerodynamic Theory, vol. III, Springer, Berlin, 1935, p. 34.
[55] R.S. Anderson, P.K. Haff, Science 241 (1988) 820.
[56] F. Rioual, A. Valance, D. Bideau, Phys. Rev. E 62 (2000) 2450–2459.